



Sodium functionalised carbon nanofibers draw solution for a solar-thermal forward osmosis water desalination system

Aondohemba Aende, Jabbar Gardy, Mohamed Edokali, David Harbottle, Ali Hassanpour^{*}

School of Chemical and Process Engineering, Faculty of Engineering and Physical Sciences, University of Leeds, Leeds LS2 9JT, West Yorkshire, UK

ARTICLE INFO

Keywords:

Water desalination
Solar thermal forward osmosis
Draw solution
Osmotic pressure
Carbon nanofibres, Solar energy

ABSTRACT

Desalination offers the potential to bridge the demand-supply gap in the increasing global freshwater scarcity, with the forward osmosis (FO) technique appearing as an attractive solution amongst the various desalination technologies. However, the significant energy demand encountered during the draw-solute recovery process in FO desalination is considered the major anathema amongst other contending factors for which the allure of FO as a desalination technology becomes questioned. Consequently, a potentially innovative draw solution (DS) regeneration strategy, enabling the circumvention of the energy requirements associated with the recovery stage in FO desalination, is evaluated. The direct solar thermal FO (DSTFO) desalination concept is predicated on engineering and applying solar absorptive DS to directly leverage solar energy for solute recovery without recourse to electric power. In advancing the DSTFO concept, this study fabricated and evaluated a novel and highly osmotic sodium functionalised carbon nanofibres (Na/CNF) DS having a high osmotic pressure (93.9 bar), a low reverse solute flux (RSF) of 0.24 gMH, and a photothermal conversion efficiency of 63.49%, resulting in an evaporation rate of 1.85 kg/m²/hr under 2 suns of solar radiation. The DSTFO strategy offers a low-cost solution for enhancing water recovery and decreasing energy use in FO desalination systems.

1. Introduction

The twofold problem of freshwater scarcity and energy insecurity has continued unabatedly to scourge humanity in the 21st century. The competing demands of growing freshwater needs from an increasingly growing population worldwide, climate change, and growing economic and industrial developments are all principal contributors, amongst other contending factors (Kim et al., 2013; Aende et al., 2020). Saltwater desalination is considered an alluring solution leverageable to increase the global supply of potable freshwater due primarily to the reams of continental saltwater sources—seawater, brackish water, and groundwater—that abound (Aende et al., 2020; Dey and Izake, 2015). However, notwithstanding the numerous desalination technologies exploited over the years to harness drinkable water from saltwater sources, these technologies are generally considered cost prohibitive and out of reach due to their high energy requirements, amongst other complexities (Aende et al., 2020; Bank, 2019). Therefore, exploring alternative desalination technologies requiring less energy, fostering cost savings, improving air quality, and enhancing energy security is highly imperative. Forward osmosis (FO), a process that uses natural osmotic pressure

as its driving force, has recently drawn considerable attention in ongoing research to find innovative desalination solutions that offer improved energy efficiency. The osmotic pressure difference between two solutions with varying concentrations impels water permeation across a semipermeable membrane from a low-concentration feed solution (FS) to a more concentrated draw solution (DS), thus diluting the DS in the process (Aende et al., 2022). FO's appeal stems from its low fouling propensity, ability to treat complex effluents, and, more importantly, the perspective that it does not require external energy or pressure to drive the process, especially in standalone FO systems, and thus offering energy reduction potentialities (Aende et al., 2022; Bell et al., 2016). However, whilst standalone FO evolves without energy strictures as it relies on osmotic pressure, it cannot on its own be deployed for desalination purposes to obtain potable water. The reason is due primarily to the requirement of a second step or technique to recover the draw solutes and extract pure water, at which point the system is oppugned (Aende et al., 2022; Shaffer et al., 2015). Numerous draw solutes and the applicable recovery methods have undergone diverse research evaluations to extract pure water from diluted DS, and many are still under ongoing research. More often, thermal regeneration

^{*} Corresponding author.

E-mail address: A.Hassanpour@leeds.ac.uk (A. Hassanpour).

<https://doi.org/10.1016/j.cherd.2024.01.017>

Received 20 September 2023; Received in revised form 21 December 2023; Accepted 10 January 2024

Available online 12 January 2024

0263-8762/© 2024 The Author(s). Published by Elsevier Ltd on behalf of Institution of Chemical Engineers. This is an open access article under the CC BY license (<http://creativecommons.org/licenses/by/4.0/>).

methods and membrane processes such as reverse osmosis (RO), nanofiltration (NF), membrane distillation (MD), ultrafiltration (UF), and microfiltration (MF) are commonly deployed for DS reconcentration evaluations (Kim et al., 2013). The selection of the applicable recovery techniques is often contingent on the type of DS employed in the FO process (Aende et al., 2020). A previous work by the authors provided a comprehensive overview of various DS types and the relevant recovery strategies applied (Aende et al., 2020). The draw solute recovery process in FO desalination tends to be where a significant amount of energy demand for the entire FO process is used up (McCutcheon and Elimelech, 2007). The energy demand at this stage is often greater than the minimum thermodynamic energy of recovery in desalination due to the energy deficiencies of the secondary techniques deployed in the recovery process, which inevitably rub off on the overall FO process (Aende et al., 2020; Shaffer et al., 2015). For instance, solute regeneration using RO accounted for around 19 kWh/m³ in an early pilot investigation of a hybrid FO-RO system out of the system's total specific energy consumption (SEC) of 25 kWh/m³ (Cath et al., 2005; Zou et al., 2016). Even so, RO, the most common recovery method, typically requires around 2.5–5 kWh/m³ of electricity for desalination, depending on size, location, and the source water's salinity, among other specifics (Kim et al., 2013). Moreover, an independent study demonstrated that hybrid FO systems employing pressurised membrane filtration mechanisms for solute recovery have comparable SEC to standalone RO systems, regardless of the DS type utilised (Mazlan et al., 2016).

Several studies employing different approaches have emerged from ongoing attempts to improve the energy efficiency of hybrid FO desalination systems. Scholarly research utilising ammonia bicarbonate as DS applied moderate heat to separate the DS into NH₃-CO₂ gases, which were then recycled through distillation whilst extracting product water from the diluted DS (McCutcheon et al., 2005). Following this research, several studies investigating thermally recoverable DS were reported (McCormick et al., 2008; Kim et al., 2012). Further research on the energy efficiency of the NH₃-CO₂ system revealed that only a multi-stage distillation column utilising waste heat could improve the system's solute separation energy efficiency (McGinnis and Elimelech, 2007). Whilst the NH₃-CO₂ system offers potential energy-saving using waste heat during the solute separation stage, complete CO₂ re-dissolution is challenging and can increase energy consumption and costs, ultimately affecting the overall efficiency (Kim et al., 2013). Furthermore, the product water will require further treatment from odour which will incur extra costs (Mazlan et al., 2016). It also follows that NH₄HCO₃ as a DS possesses a high tendency to back diffuse into the FS, which can pose a risk to the FO system (McGinnis and Elimelech, 2007; Hancock and Cath, 2009; Alturki et al., 2013). Additionally, the NH₃-CO₂ system's efficiency can be reduced and might require additional solutions at an extra cost due to fouling issues with the columns (Hancock and Cath, 2009). Therefore, exploring solute recovery processes for FO desalination that are simple, require less energy, assure product water quality, and optimise equipment efficiency is critical.

Integrating solar energy into FO desalination represents a crucial step towards sustainably addressing the energy deficit in FO technology for potable water processing. Stimuli-responsive hydrogels have shown potential for solar-assisted FO water recovery; however, their water recovery efficiency remains a significant challenge (Long et al., 2018). Therefore, this work's primary focus is to explore the direct solar thermal FO (DSTFO) desalination concept using a solar absorptive nanofluid capable of generating high osmotic pressure for enhanced water flux and achieving product water recovery by leveraging solar energy without its usable form of electric current. Specifically, the work will synthesise and evaluate a carbon-based nanofluid for DSTFO desalination using a purposely designed passive solar device to facilitate DS regeneration. In addition, performance evaluation parameters, including osmotic pressure, water flux, reverse solutes flux (RSF), specific reverse solute flux (SRSF), solar-thermal conversion efficiency, water evaporation rates, and water quality, will be examined and compared with the literature. A

novel sodium functionalised carbon nanofibres (Na/CNF) DS is synthesised, characterised, and evaluated to advance the concept of the DSTFO desalination process herein, employing a fabricated cone-shaped condenser device. The novel Na/CNF DS could be more stable and exhibit a higher osmotic pressure, and it is feasibly recoverable by leveraging solar energy without its usable form of electric current.

2. Materials and methods

2.1. Material consideration

Using carbon nanofibre material in this work's nanofluid predicated different advantages, including ease of conversion into usable forms through a simple process, and possession of much-enhanced stability under solar irradiation than polymers and other carbon-based materials. Other advantages include their ease of conversion into nanoscale suitable for solar thermal implementation, scalability, non-hazardous as well as applicability in wastewater treatment, amongst other benefits. In addition, sodium ions offer the advantages of high hydrophilicity and a high degree of osmotic activity owing to a combination of factors. These include tightly packed hydration shells due to their small ionic size, stronger ion-water interactions due to their high charge density, a positive charge that attracts the negatively charged oxygen atoms in water molecules, and high solubility in water.

2.2. Synthesis of novel Na/CNF nanofluid DS

Fig. 1 illustrates the novel Na/CNF DS fabrication process schematic. In this process, a 250 mL round bottom flask was carefully charged with an 80 mL aqueous solution of nitric acid (HNO₃) and sulphuric acid (H₂SO₄) in a molar ratio of 1:3. After that, 5 g of commercial carbon nanofibres (CNF) powder was carefully added to the acid mixture. The suspension was then put under refluxing for 6 hrs at 70 °C with constant and gentle stirring at 250 rpm. Afterwards, the suspension mixture was filtered and washed with deionised (DI) water several times before being oven-dried in a vacuum oven at 80 °C overnight. The as-treated CNF powder was then dispersed in a 50 mL aqueous solution of 0.05 M sodium dodecyl sulphate (SDS) and mixed using a probe sonicator for 30 min. Subsequently, the sonicated SDS-CNF suspension was carefully transferred into a 1 L round-bottom flask and heated to 80 °C for 4 hrs whilst stirring continuously at 250 rpm. Following that, 250 mL of a 0.5 M NaOH aqueous solution was gradually added to the reaction mixture whilst gently stirring at 250 rpm under reflux for another 4 hrs to obtain a Na/CNF composite solution. The Na/CNF solution obtained was then centrifuged using the Thermo Fisher Megafuge at 15,000 rpm for 30 min to separate the Na/CNF solid particles from the solution. Furthermore, 100 mL of a 0.05 M hydrochloric acid solution was added to a 250 mL beaker containing the solid particles, and the suspension was stirred gently on a magnetic stirrer at 250 rpm overnight. The solid particles were then filtered using 0.5 µm filter paper and repeatedly washed until no chloride ions were detected using an AgCl solution as an indicator and until the pH of the filtrate reached 7. The resulting Na/CNF mixture was then oven-dried at 120 °C overnight and ground into a fine powder. Finally, 1 g of the Na/CNF powder was dispersed in 100 mL of DI water to prepare a 1% stock solution (wt/vol%). From this, 0.075 and 0.1 wt/vol% of the stock solution were measured and put aside for FO performance assessments.

2.3. Characterisation techniques

The Bruker D8 X-ray diffraction (XRD) with Cu K radiation ($\lambda = 1.5418$) was employed to examine the structural and crystal phase analysis of the Na/CNF sample. The instrument was operated and maintained at 40 kV and 40 mA applied current, respectively. The sample was scanned at a 2θ angle range of 10 to 70° at 1 sec per step with a step size of 0.0495°. Cold field-emission scanning electron

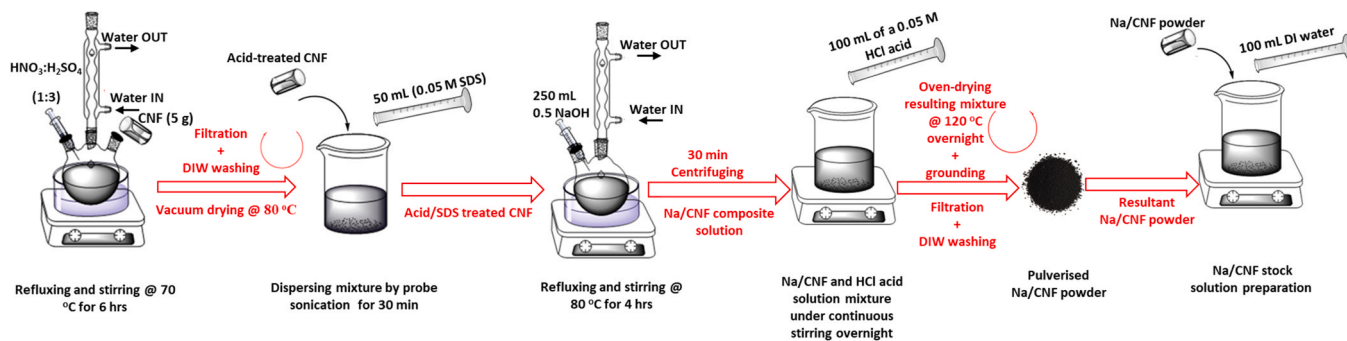


Fig. 1. A schematic representation of the Na/CNF DS fabrication process.

microscopy (Hitachi SU8230 CFE-SEM) was employed to analyse the elemental composition, surface morphologies, and elemental mapping of the Na/CNF sample. A transmission electron microscopy (TEM) system (FEI Titan3 Themis 300), integrated with a Gatan OneView 16 Megapixel CMOS digital camera, was applied to gather bright-field TEM images. A droplet of Na/CNF material in acetone, placed on a carbon-coated copper grid for a micropipette, was analysed using the system. The functional groups in the synthesised Na/CNF material were analysed in the 525–4000 cm^{-1} range at room temperature using an attenuated total reflection (ATR) approach on a Nicolet™ iS10 FTIR spectrometer (Thermo Scientific™) with a resolution of 4 cm^{-1} .

The prepared Na/CNF material's thermal stability was analysed using thermo-gravimetric analysis (TGA) equipment (Mettler Toledo, TGA/DSC-3). The analysis used a nitrogen purge gas (50 mL/min) under a constant flow rate, a temperature range of 30 to 900 °C, and a heating rate of 10 °C/min. Additionally, the charge stability of the Na/CNF DS was assessed through zeta potential measurements utilising a Zetasizer (Malvern Instruments, UK). The osmolality of the Na/CNF sample was measured using the 3250 model Osmometer (Advanced Instruments, USA) to determine the sample's osmotic pressure at varying concentrations.

2.4. FO experiment

The FO experiment was conducted in the FO mode (AL-DS) at room temperature with a crossflow cell unit (CFO42D, Sterlitech Corporation Inc, USA) with an active membrane area of 42 cm^2 . A constant 1280 mL/min flow rate was maintained across the FS and DS tanks, using two Masterflex Console Gear Pumps (Cole Palmer, USA) to moderate the flow volumes. Scheme S1 in the supplementary information depicts the overall schematic of the FO setup used for the experiment.

The weight change in the feed tank containing a 1.0 M NaCl solution was continuously measured at 5 min intervals using a calibrated analytical balance (A&D EX300i, USA) over a 60 min experimental run. The water flux across a commercial flat sheet cellulose triacetate (CTA) membrane (FTSH2O™) was determined using the values of the volumetric weight changes applying the formula:

$$J_w = \frac{\Delta m}{\rho_f \Delta t} = \frac{\Delta V}{\Delta t} \quad (1)$$

where J_w is the permeate flux in $\text{L}/\text{m}^2/\text{h}$ (LMH), Δm is the change in mass of the FS over time, ρ_f is the density of water, Δt is the change in time (h), ΔV is the volumetric change (L) of the FS, and A is the active membrane area (m^2) of the CTA membrane. During the FO experimental run, the conductivity of the draw stream was monitored continuously at every 5 min interval with a calibrated benchtop conductivity metre (VWR Symphony™). The measured conductivity data (mS/cm) were converted to concentration (Fipps, 2003) and used to estimate the RSF from the equation:

$$J_s = \frac{(C_t V_t - C_o V_o)}{\Delta t} \quad (2)$$

where J_s is the RSF ($\text{g}/\text{m}^2/\text{h}$), also expressed as gMH , C_o and C_t are DS concentrations at the start of the experiment and Δt respectively, V_o and V_t are the DS volumes (L) at the beginning and Δt , respectively (Amjad et al., 2018).

3. Results and discussions

3.1. Characterisation of Na/CNF DS material

Fig. 2(a) depicts the FTIR spectra obtained for Na/CNF sample. The broad peak at $\sim 3501 \text{ cm}^{-1}$ is identical to the -O-H stretching vibrations of the -C-OH and -COOH functional groups on the surface of CNF (Aende et al., 2022; Pavia et al., 2014). The sharp peaks at ~ 2924 and $\sim 2855 \text{ cm}^{-1}$ correspond to the -C-H (asymmetrical/symmetrical) stretching vibrations of the $>\text{CH}_2$ functional groups (Nandiyanto et al., 2019). The peak at $\sim 2613 \text{ cm}^{-1}$ is associated with the -O-H stretching vibration of the -COOH group occurring between the 3400–2400 cm^{-1} frequency band (Pavia et al., 2014). The weak peak at $\sim 1976 \text{ cm}^{-1}$ is attributable to the -C-H bending vibration associated with aromatic compounds in CNF appearing between 2000–1650 cm^{-1} frequency region (Pavia et al., 2014; Nandiyanto et al., 2019). The sharp peak at $\sim 1632 \text{ cm}^{-1}$ corresponds to the -C=C- stretching vibration associated with the alkenes (Nandiyanto et al., 2019). Another sharp peak at $\sim 1383 \text{ cm}^{-1}$ corresponds to the -O-H bending associated with -C-OH and -COOH functional groups appearing between the 1410–1310 cm^{-1} region (Nandiyanto et al., 2019). The peak at $\sim 1260 \text{ cm}^{-1}$ is characteristic of OH in-plane bending of a primary or secondary alcohol and hydroxyl groups occurring between 1350–1260 cm^{-1} range, whilst the band at $\sim 1106 \text{ cm}^{-1}$ connotes -C-O- stretching vibration of secondary alcohols (Pavia et al., 2014; Nandiyanto et al., 2019). The band at $\sim 802 \text{ cm}^{-1}$ indicates skeletal -C-C- vibration absorptions from the 1300 to 700 cm^{-1} range. Finally, the band at $\sim 621 \text{ cm}^{-1}$ relates to the OH out-of-plane bending of alcohol appearing from the 720–590 cm^{-1} absorptions region (Nandiyanto et al., 2019). Furthermore, the diffraction peaks at 2θ set values of 27° and 44° corresponding to (002) and (101) planes as shown in Fig. 1(b) are characteristic patterns attributable to carbon and sodium.

Fig. 3 depicts the bright-field TEM images of the Na/CNF DS sample material. The TEM images reveal cylindrical fibres with rough inner and external edges reminiscent of CNF. The rough surface edges of the CNF as indicated by blue arrows in Fig. 3b-i provide sites for covalent and non-covalent modifications or a combination of both to achieve multiple essential functionalities. This observation corroborates earlier reported findings (Aende et al., 2022). Also displaying are some clustered morphologies (see red arrows in Fig. 3a-ii and b-iii) indicative of metal ions (possibly sodium) which appear closely bounded around some CNF. Furthermore, a cold field emission scanning electron microscopy

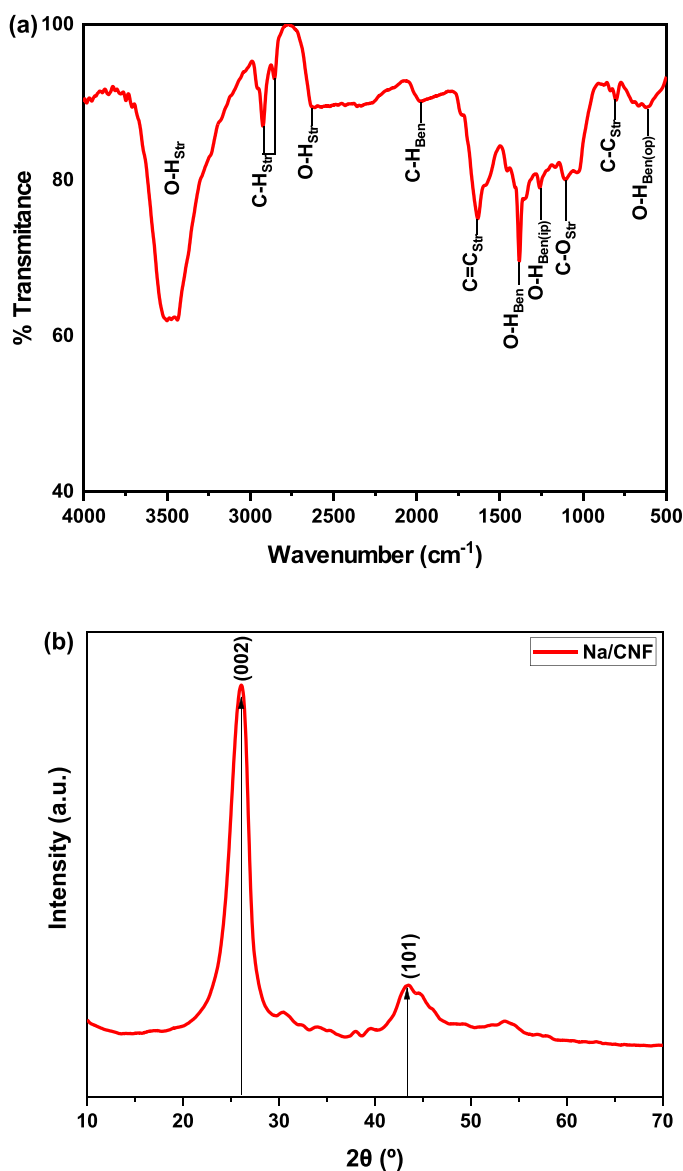


Fig. 2. (a) FTIR spectra (b) XRD patterns for the novel synthesised Na/CNF material. (coloured).

(CFE-SEM) analysis examined the overall morphology of synthesised Na/CNF DS. Fig. 3(c) displays the SEM micrographs of the Na/CNF draw solute material at various magnifications, displaying some fibrous morphologies (c-i) indicative of pristine CNF, and (c (ii-iii)) CNF appearing closely bound up with each other following the doping with NaOH.

The EDS analysis of the Na/CNF sample shown in Fig. S2. (a) confirmed the presence of sodium, carbon, and oxygen elements in the DS functional material, indicating successful Na/CNF material synthesis. The elemental mapping of the sample, as represented in Fig. S2. (b), displayed clustered NPs with the Na^+ appearing evenly dispersed and imbricating the CNF. The analysis demonstrates further the successful modification of the CNF with NaOH. CNFs are intrinsically hydrophobic without surface coatings (Hernández-Hernández et al., 2010). However, modifying the CNF surfaces with Na^+ through NaOH greatly enhanced its hydrophilicity, improving its osmotic pressure. Fig. S3 displays the zeta potential distribution profile for the Na/CNF DS. The material exhibited a zeta potential value of -31.9 mV, indicating good charge stability.

3.2. Osmotic pressure analysis

Fig. 4 represents the osmolality of two different concentrations of the Na/CNF sample and that of a solution of 1.0 M NaCl. The final osmolality reading for each sample concentration was determined by averaging two osmolality readings. Observably, the samples' osmolality varies depending on the different concentrations. Furthermore, the Na/CNF sample with concentrations of 0.075 and 0.1 wt/vol% gave osmolality of 2548 (64.9 bar) and 3684.5 mOsmol/kg (93.9 bar), respectively. Similarly, the osmolality of 1.0 M NaCl solution was determined to be 1804 mOsmol/kg (45.96 bar). Instructively, the DS concentrations of 0.075 and 0.1 wt/vol% produced significant osmotic pressures, contrasting with other DS investigated in the literature at considerable DS concentrations in several studies (Ling and Chung, 2012; Ban et al., 2019; Khazaie et al., 2021).

The enhanced osmolality exhibited by the Na/CNF is further aided and facilitated by the diverse functional groups within its fold incorporated by design, coupled with its augmented ionisation where sodium carboxylate groups dissociate into more ions per unit, unlike NaCl, amongst other factors. The potential for multiple carboxylate groups on each CNF molecule to ionise can result in a higher ion count, thereby increasing osmolality. Conversely, the NaCl solution, undergoing simple dissociation into Na^+ and Cl^- ions, does not exhibit the intricate interactions and colloidal properties unique to Na/CNF. As a result, it lacks the enhanced osmotic effects resulting from the physical and chemical characteristics ingrained in Na/CNF.

3.3. FO evaluation

Different parameters, including osmotic pressure, water flux over time, average water flux, RSF, and SRSF, were examined to ascertain the FO functionality of the Na/CNF DS. Fig. 5(a) shows the cumulative change in permeate volume over time, observed to rise incrementally, depicting weight loss in the feed tank. The water flux, RSF, and electrical conductivity (feed tank) change over time during the FO experiment for the 0.1 wt/vol% DS and 1.0 M NaCl FS are shown in Fig. 5(b, c, and d), respectively. The results depict a high initial water flux of 7.2 LMH within the first 10 mins of the FO process, which declines and stabilises relatively after, indicating negligible membrane fouling (Cath et al., 2010). The high initial water flux is due to a high DS concentration at the start of the FO experiment; at this point, the osmotic driving force is very active, thus eliciting a high permeate flux (Amjad et al., 2018). The feed conductivity increased over time, possibly due to the diffusion of some DS solute into the FS, as in osmotically driven membrane processes (Cath et al., 2010), whilst the RSF revealed some negative variations during the initial stages, indicating solute transport into the DS from the FS (Aende et al., 2022; Coday et al., 2013). Negative RSF variations could have resulted from the significant initial driving force and thus higher water flux experienced at the beginning of the FO run, which causes more FS total dissolved solids (TDS) to be transported to the membrane surface by convection, with some of these ions then diffusing into the DS. The average RSF and SRSF values obtained via the 0.1 wt/vol% DS concentration were 0.24 gMH and 0.09 g/L, which are low and thus less significant. We used the 0.1% DS concentration to evaluate cumulative permeate volume change, RSF, SRSF and other system evaluations based on our previous study for comparisons. Fig. 5 (e) illustrates the average water flux of the Na/CNF DS at varying concentrations relative to 1 M NaCl and DI water as the FS, respectively. The result revealed an average water flux of 4.13 LMH at 0.1 wt/vol% DS concentration using DI water FS, relative to the average water fluxes of 2.65 and 1.71 LMH obtained for the DS concentrations at 0.1 wt/vol% and 0.075 wt/vol%, respectively. The concentration of dissolved ions in a solution determines its ionic strength (Bai et al., 2011). In FO operations, the concentration or osmotic pressure of the FS directly affects the net driving force (Phuntsho et al., 2013). However, no counterionic strength is present when using DI water as the FS, which may explain the

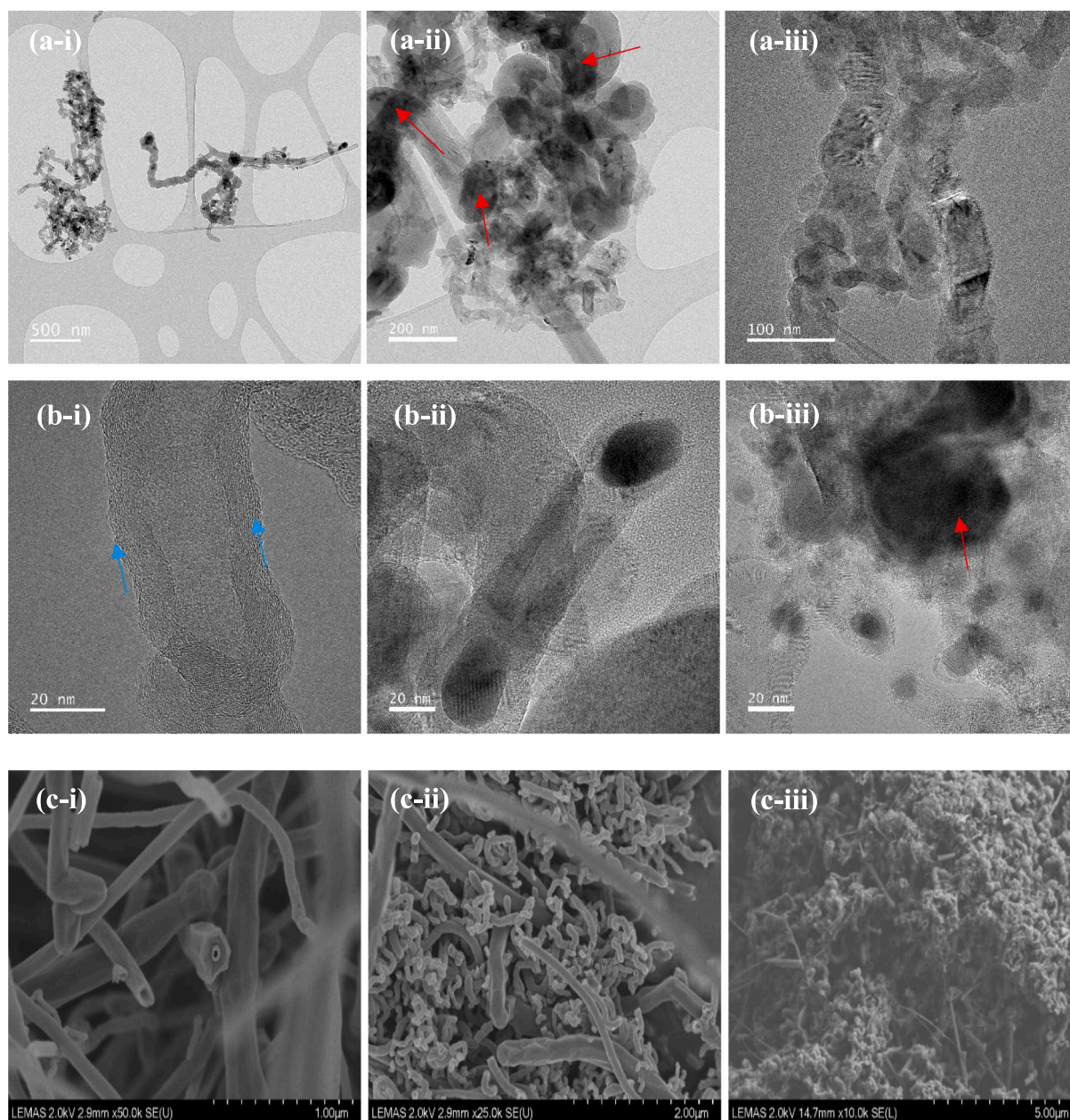


Fig. 3. (a–b) TEM images and (c) CFE-SEM micrographs of the Na/CNF sample at different magnifications. (coloured).

higher water flux obtained.

The observed decrease in water flux over time in this work could be attributable to dilutive internal concentration polarisation (ICP), in which salts migrating from the DS within the porous support layer of the membrane become diluted by water diffusing from the FS to the DS. When and where this phenomenon occurs over time, the system's overall effective driving force becomes compromised, consequently eliciting an overall drop in water flux (Cath et al., 2010). Another contributing factor to the decline in water flux could be the dilution of the DS by the permeate water from the FS, resulting in the gradual decrease in the net osmotic pressure across the membrane over time during the FO process, thus lowering the water flux (Bai et al., 2011). Compared to the K/Fe₃O₄/CNF DS previously examined in the literature, which had an osmotic pressure of 86.1 bar and an average water flux of 2.18 LMH (Aende et al., 2022), the Na/CNF DS in this study demonstrated a higher osmotic pressure (93.9 bar) and a greater average water flux (2.65 LMH). This differential osmotic performance is attributable to the influence of ion size and charge density of the Na⁺

and K⁺ species in the samples (Cannon et al., 2012; Collins, 1997). In this case, Na⁺, having the smallest ionic radius, the highest charge density, and more solubility than K⁺, exhibits more osmotically active behaviour and draws more water molecules. However, regarding the RSF, the value was higher in the Na/CNF DS (0.24 gMH) compared to the K/Fe₃O₄/CNF DS (0.10 gMH). The smaller ionic radius and higher charge density of the Na⁺ than the K⁺ may explain this difference. It allows the Na⁺ to diffuse more quickly through an aqueous solution, leading to a higher concentration of Na⁺ near the membrane surface, thus increasing the likelihood of RSF (Zou et al., 2019; Zhao and Zou, 2011). K⁺, on the other hand, has a bigger ionic radius and a lower charge density, decreasing its propensity to interact with the membrane and thus reducing RSF (Zou et al., 2019). Therefore, this highlights the criticality of understanding DS material properties, amongst other system parameters, for an effective FO desalination system. Overall, a DS satisfying nontoxicity, ease of fabricating, and cost-effective separability from the permeate whilst consuming minimal energy is highly desirable for FO desalination applications. Crucially, a DS offering considerable

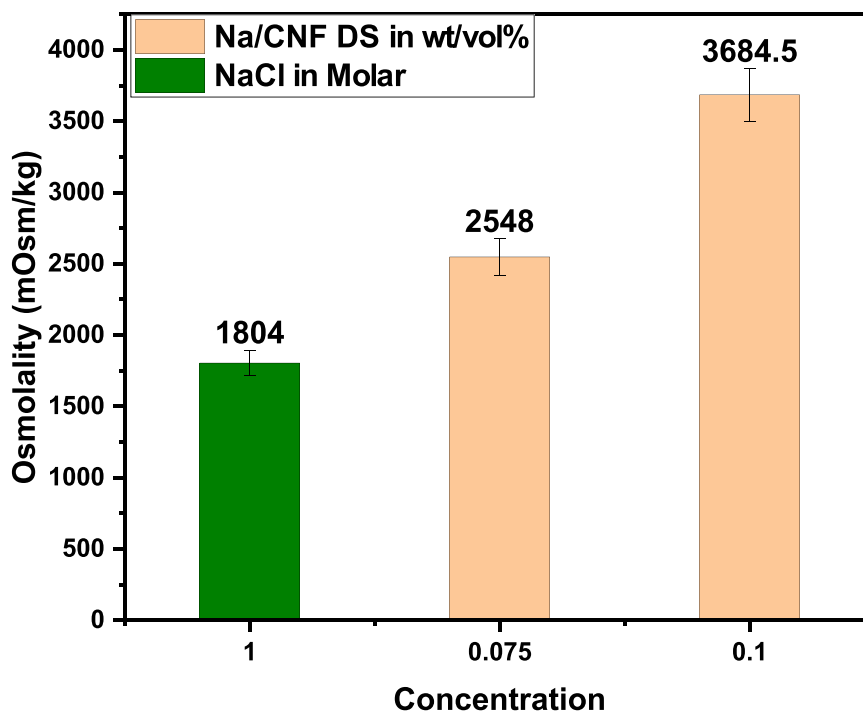


Fig. 4. The osmolality of Na/CNF DS at varying concentrations and 1.0 M NaCl solution. (coloured).

driving force at low concentration can significantly reduce overall costs.

4. Solar-thermal performance and DS regeneration experiment

4.1. Fabrication of passive solar evaporation apparatus

For enhanced water recovery from the DS regeneration leveraging direct solar energy, a passive solar device was fabricated and investigated for DS reconcentration and product water recovery. Fig. S4. shows the schematic arrangement of the proposed DS regeneration unit. The apparatus features a pair of 23 mm deep Pyrex reservoirs at the device's base. The interior vessel (internal diameter = 46 mm, external diameter = 62 mm) warehouses the DS and is enclosed within an exterior container (inner diameter = 50 mm, outer diameter = 70 mm), which holds the condensates from the evaporated DS. The top of the reservoirs is then covered with a 1.4 mm thick transparent right circular silica glass cone-shaped condenser plate with a tilt angle of 60° so trapped water vapours can descend more efficiently, enabling improved condensate collection. In addition, three holes were drilled through the reservoirs at optical depths of 3, 7, and 11 mm from the bottom-top to allow the running through of K-type thermocouple (TC) wires, thereby facilitating temperature rise measurements. This design could limit heat loss within the system by helping to trap and prevent heat from exiting, allowing the system to maintain a higher temperature, and improving the evaporation efficiency and overall water recovery process.

4.2. DS regeneration experiment

The second stage of the FO desalination process involves DS regeneration and product water recovery. Herein, the Na/CNF nanofluid DS sample is evaporated under solar irradiation to obtain product water. Fig. S5. represents the schematic diagram of the setup used for the evaporation experiment. A class AAA-certified solar simulator (Newport Co.) having a 450 W xenon lamp and an air mass 1.5 global (AM 1.5 G) optical filter was utilised as a light source to simulate the direct solar spectrum with the sun. Three K-type TC wires connected to a data logger were inserted through the external reservoir into the 46 mm inner

diameter reservoir vessel at 3, 7 and 11 mm along the sample's optical depth to measure the sample's temperature rise. In addition, a fourth TC wire linked to the data acquisition system was projected outside but not in contact with the evaporation device to record the surrounding temperature.

A flexible feed line delivers 20 mL of the nanofluid into the DS holding reservoir. The sample is then heated up under solar irradiation whilst ensuring that the top of the reservoirs is hermetically sealed with the cone-shaped condenser plate using a sealant to prevent side leakage of water vapours during the evaporation-condensation process. As the DS becomes heated under solar flux, its surface temperature rises to the point where the water molecules inside it begin to evaporate, resulting in tiny droplets of water vapour that become trapped inside the device on the walls of the glass condenser plate, leaving behind the solute material. Consequently, the tiny droplets gradually clump over time, developing into larger droplets that condense and glide down the condenser plate due to surface tension. They are eventually drained into the bottom of the external reservoir, collected as clear condensates into a measuring cylinder via a collecting tube, and allowed to cool under ambient environmental conditions before water quality tests. The weight change of the sample during a 60 min exposure to 2 suns (2 suns = 2 kWh/m²) of simulated radiation was measured using a digital analytical balance (Discovery DV144C, Ohaus Corporation, USA, with a sensitivity of 0.1 mg). Radiation flux changed the Na/CNF nanofluid sample's temperature and mass during the experiment, and a data capture system, LabVIEW, was used to record the samples' real-time mass and temperature changes and continually log the results on a computer every second of the operation. Following product water extraction from the DS under solar irradiation, the DS became somewhat concentrated as the solute particles began to thicken, resulting in a modest increase in concentration to 1.340 mg/L.

4.3. Solar-thermal performance of the Na/CNF DS nanofluid

The nanofluid DS's solar-thermal performance was related to its solar photothermal conversion efficiency and water evaporation rate, as measured by the change in mass of the samples over the irradiation time.

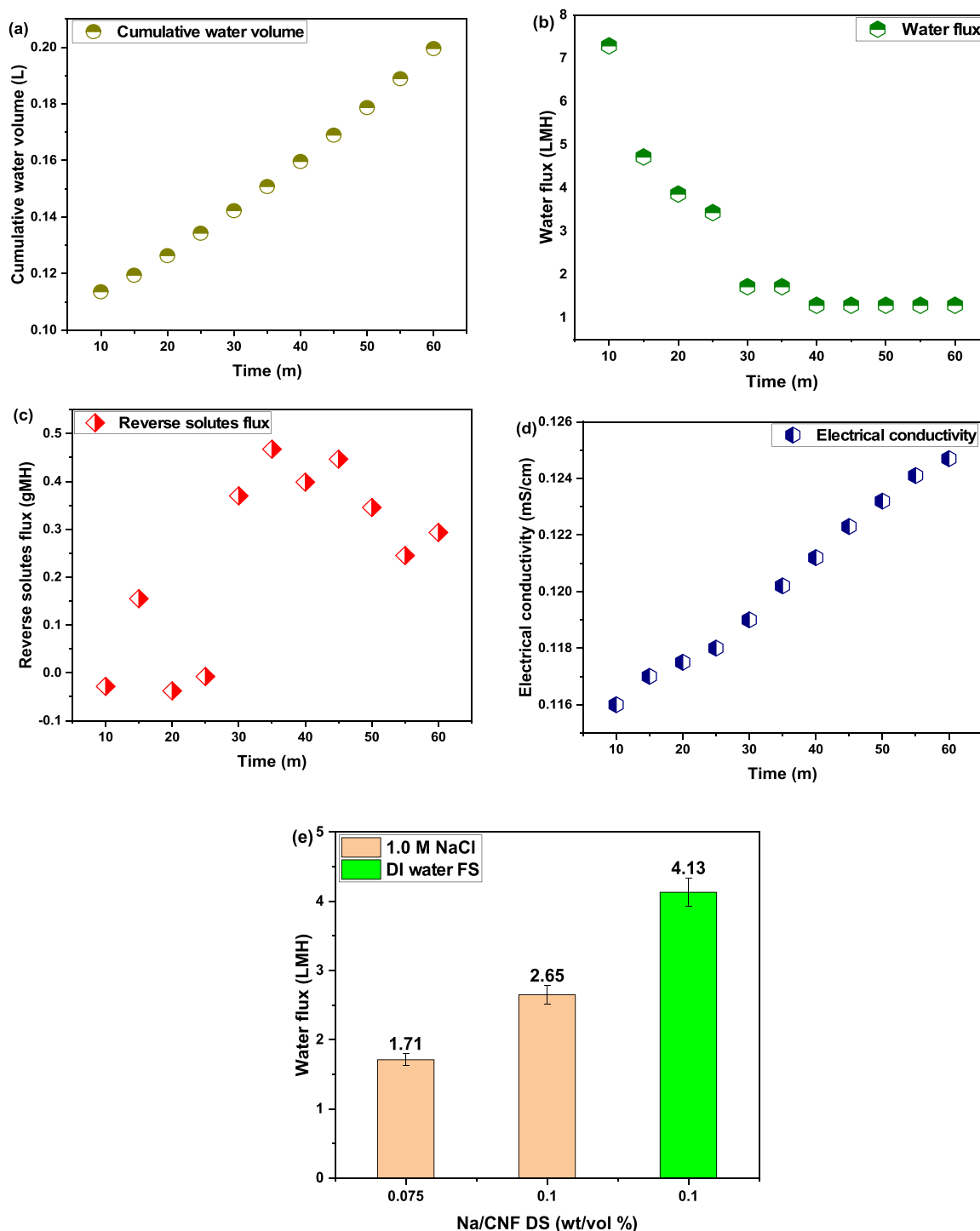


Fig. 5. (a) Cumulative permeate volume over time and (b) water flux and (c) reverse salt flux (d) electrical conductivity of the Na/CNF DS as a function of time and (e) average water flux against varying concentrations of Na/CNF DS. (coloured).

These crucial parameters are instrumental in evaluating the operational viability of the nanofluid. The solar photothermal conversion efficiency measures the nanofluid's capacity to convert solar irradiation into heat which is critical for generating thermal energy within the fluid. Moreover, the nanofluid's evaporation rate is linked directly to the amount of recoverable water within a specific period. Fig. 6(a-b) depicts the temperature changes in the 1.0 M NaCl solution and the 0.10 wt/vol% Na/CNF nanofluid samples under exposure to radiation flux for 3600 sec. In Fig. 6(a), the temperature appeared to rise almost uniformly, possibly because most radiation was not absorbed or reflected off the sample

volume due to its transparent nature and inefficient solar absorption capacity (Amjad et al., 2018). Conversely, there appears to be an uneven temperature distribution along the optical depth of the Na/CNF nanofluid, as shown in Fig. 6(b). When exposed to 2 suns of solar radiation for 3600 sec, there was a significant temperature differential between the sample's top and lower optical depths. Over the varying depth of the nanofluid, the surface fluid volume became heated, with the top TC temperature rising swiftly and progressively to 46 °C. The temperature of the underlying fluid layer also increased, but slowly with increasing depth, as the heat flux penetrated the bulk fluid volume. The heat

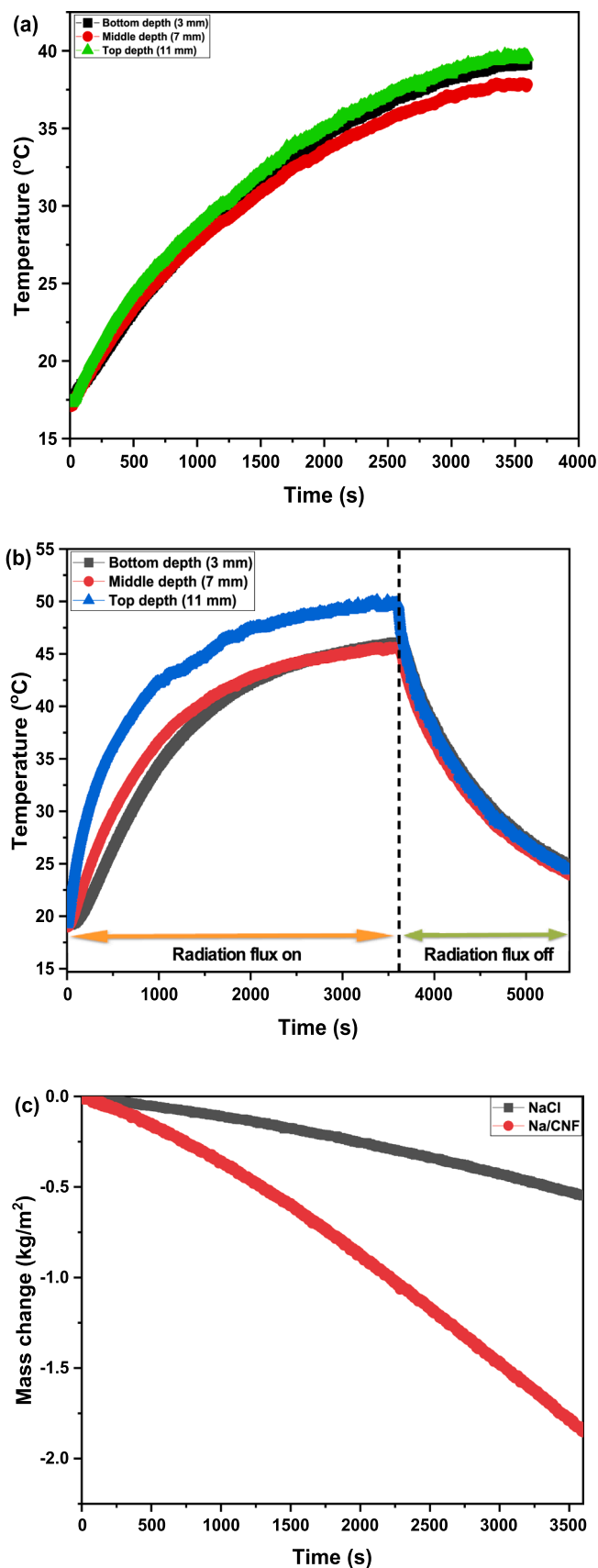


Fig. 6. Temperature distribution profile over the optical depth of (a) 1 M NaCl solution (b) 0.1 wt/vol% Na/CNF nanofluid when irradiated under 2 suns and (c) Evaporation rate profile of 1 M NaCl solution and 0.1 wt/vol% Na/CNF nanofluid over time. (coloured).

generated by the radiation flux causes a continuous rise in vapour as the fluid temperature rises. As a result, the ensuing water vapour departing from the bulk fluid volume descends the condenser as clear condensates until the radiation flux gets switched off. With the lights out, the fluid's surface temperature dropped precipitously whilst the bulk fluid temperature began to stabilise. The increasing temperature rise relates to the enhanced radiation absorption and heating at the surface because of the blackbody nanofluid, resulting in the surface layer absorbing more solar energy than the layer beneath it.

The solar photothermal conversion efficiency (η) of the Na/CNF nanofluid was evaluated using the relation given in (Ma et al., 2021):

$$\eta = \frac{m[C_{pS}(T - T_o) + H_{LV}]}{E_{Input}} \times 100\% \quad (3)$$

where m is the evaporation rate ($\text{kg}/\text{m}^2/\text{h}$), E_{Input} denotes the normal direct solar irradiation input ($2000 \text{ W}/\text{m}^2$), C_{pS} denotes specific heat capacity of solution [$C_{p \text{ Na/CNF}} = 2.76 \text{ kJ}/\text{kg}/\text{K}$ measured from differential scanning calorimetry (DSC), and $C_{p \text{ water}} = 4.2 \text{ kJ}/\text{kg}/\text{K}$ at 1 atm, respectively], T and T_o are the surface average temperature (Na/CNF = ~ 43.82 , NaCl = ~ 32.37 °C) and the initial average temperature (Na/CNF = ~ 17.86 , NaCl = ~ 15.97 °C), and H_{LV} is the water enthalpy of vaporisation at the surface equilibrium average temperatures (2396.8 kJ/kg at 43.82 °C, and 2424.2 at 32.37 °C) from The Engineering ToolBox 2022 Water – Heat of Vaporisation vs. Temperature. Here we assume the C_p of water for NaCl solution, and H_{LV} of water applicably.

Fig. 6(c) shows the evaporation rate profile of the 1.0 M NaCl solution and the 0.1 wt/vol% Na/CNF nanofluid, respectively. The blackbody CNF in the nanofluid promoted the sample's solar adsorption across the solar spectrum and, by extension, evaporation performance, achieving a water evaporation rate of $1.85 \text{ kg}/\text{m}^2/\text{hr}$ and a corresponding solar thermal conversion efficiency of 63.49% as against NaCl solution's $0.55 \text{ kg}/\text{m}^2/\text{hr}$ and 18.97%.

Table 1 compared the photothermal performance of the DS nanofluid in this work with that of other carbon-based nanofluids under volumetric heating. Unlike previous studies reported in the literature, some of which utilised high radiation flux ($\geq 10 \text{ W}/\text{m}^2$), this work achieved a 63.49% photothermal conversion efficiency and an evaporation rate of $1.85 \text{ kg}/\text{m}^2/\text{hr}$ with modest solar irradiance ($2 \text{ kWh}/\text{m}^2$) and low nanofluid concentration (0.10 wt/vol%). In July, the average number of sunshine hours per day in Leeds is roughly 6.5 hrs (Pegasusweb, 2022). Therefore, considering the evaporation rate of $1.85 \text{ kg}/\text{m}^2/\text{hr}$ under the current experimental condition (2 suns), this theoretically equates to a daily rate of $6.0125 \text{ L}/\text{m}^2/\text{Day}$ in Leeds (assuming 1 sun, $1000 \text{ W}/\text{m}^2$).

According to the literature, the solar thermal performance of direct solar absorption systems depends on the stability and concentration of the nanofluids' volume fraction (Amjad et al., 2018, 2021). Therefore, an increase in the volumetric concentration of the DS nanofluid will bequeath the system an enhanced performance in solar thermal absorptivity, photothermal conversion efficiency, evaporation rates, and overall product water recovery. Under the current experimental conditions, for Leeds July weather (assuming 1 sun, $1000 \text{ W}/\text{m}^2$) a daily theoretical yield rate of $6.0125 \text{ L}/\text{m}^2$ per day with a 50 m^2 area could potentially cover around 300 L per day, which is close to the water consumption of a small household in the UK. This rate demonstrates that a significant amount of condensate product water is potentially recoverable using this DS regeneration system when deployed under optimal conditions. Nonetheless, we anticipate product water recovery to yield a substantially higher volume in the regions with high water scarcity where usually solar radiation and temperatures are much higher.

4.4. Product water quality analysis

Using a conductivity probe (Mettler Toledo FiveEasy™) and atomic absorption spectroscopy (AAS), we evaluated the product water's

Table 1
Comparison of essential parameters of some carbon-based volumetric solar-thermal systems.

Carbon material	System	Light source	Power density	Time	Efficiency	Evaporation rate	References
Carbon black	Volumetric	Solar simulator	10 suns	-	69%	-	(Ni et al., 2015)
Graphene	Suspension	Solar simulator	10 suns	-	68%	-	
Graphene carbon black	Suspension	Solar simulator	10 suns	-	67%	-	
CNT nanofluids	Suspension	Sun simulator	10 suns	-	46.80%	-	(Wang et al., 2016a)
Fe ₃ O ₄ /RGO	Suspension	Sun simulator	1 sun	-	70%	1.12 L/M ² /H	(Wang et al., 2016b)
GO	Suspension	Solar simulator	0.75 sun	-	48.4%	-	(Fu et al., 2017)
GO+Au 2.6 wt%	Suspension	Solar simulator	0.75 sun	-	53.8%	-	
GO+Au 7.8 wt%	Suspension	Solar simulator	0.75 sun	-	57.4%	-	
Na/CNF (0.10 wt/vol%)	Suspension	Sun simulator	2 suns	60 min	63.49%	1.85 kg/m ² /hr	This work

quality relative to various standard parameters, such as electrical conductivity, TDS, and Na⁺ concentration. Table 2 compares the analysis results to modelled saltwater and the World Health Organisation (WHO) standard recommended parametric values for potable water. The result shows that the amount of Na⁺ in the product water is less than the 200 mg/L parametric threshold value acceptable by the WHO for potable water. Thus, this may necessitate remineralisation to appropriate levels to augment its low mineral contents and chlorination for safe drinking water quality.

Overall, this work's performance results highlight the Na/CNF nanofluid and the DS regeneration system as promising. Comparatively, the passive solar device utilised in this work provides more evaporation and condensation surface area than the straight condenser, typically deployed in simple distillation setups and limited by the condensing surface area. Consequently, water collection efficiency is potentially enhanced since the cone provides a broad, curved surface for condensing vapours. More importantly, the curved cone can further improve the DS's efficiency in absorbing solar energy, raising the DS's temperature, improving evaporation rates, and making it more effective overall.

The nanofluid at 0.1 wt/vol% concentration offered a much-improved solar energy absorptivity relative to the NaCl solution. However, the Na/CNF nanofluid's photothermal conversion efficiency might be enhanced even further, even though it already exhibits excellent solar absorptivity owing to the blackbody CNF. Therefore, exploring compatible hybrid carbon nanomaterials to create DS nanofluids for DSTFO desalination processes could further enhance solar energy harnessing. Furthermore, it will be interesting to directly couple the two streams in the DSTFO concept as one integrated system and have it operated in a closed loop, where the different feeds into both streams will be continuously delivered, to understand system performance much better.

5. Conclusion

Tailoring solar thermal nanomaterials as DS to directly leverage solar energy to actuate FO desalination processes can improve the overall energy efficiency of FO desalination operations. It is a cost-competitive option for mitigating the challenge associated with the significant energy demands during the solute recovery process. Our novel Na/CNF DS showed improved photothermal conversion capability (63.49%) even at a low concentration, with up to 44.52% enhancement from the NaCl solution (18.97%) and an evaporation rate (1.85 kg/m²/hr) that compares favourably with previous results in the literature. The fabricated DS regeneration device could improve solar energy transfer to the system, and reduce heat loss, thus improving the system's efficiency. The current system will continue to undergo enhancements in future works to produce significantly improved results relative to those obtained in the present effort. Overall, potential savings in FO desalination expenses could be realised through the DSTFO concept, utilising a nontoxic DS that is simple to fabricate and, more crucially, offers a considerable driving force at low DS concentrations.

Table 2
The analysis result of condensate product water and modelled salt water.

Test parameter	WHO drinking water parametric value (Organization, 2017)	Modelled salt water	Product water
Na ⁺ concentration (mg/L)	200	22,250	2.7
TDS (mg/L)	≤ 600	51,353	*
Electrical conductivity (μS/cm)	2500	80,240	*

* Below the range of detection

Declaration of Competing Interest

The authors declare that they have no known competing financial interests or personal relationships that could have appeared to influence the work reported in this paper.

Acknowledgements

We acknowledge the support provided by Adrian Cunliffe, Karine Alves Thorne, Xialong Ma and Ben Douglas for access to the analytical equipment, Stuart Micklethwaite for performing SEM images, Zabeada Aslam for carrying out TEM analysis; and Mohammed Javed for collecting XRD data, Andrew Stockdale for the SolidWorks models, Robert Harris for the fabrication of the regeneration device and Prof. Dongsheng Wen for access to the solar simulator. A.A. thanks the Petroleum Technology Development Fund (PTDF) in Nigeria (PTDF/AAJ/250/17) for funding.

Appendix A. Supporting information

Supplementary data associated with this article can be found in the online version at [doi:10.1016/j.cherd.2024.01.017](https://doi.org/10.1016/j.cherd.2024.01.017).

References

- Aende, A., et al., 2022. A novel highly osmotic K/Fe₃O₄/CNF magnetic draw solution for salty water desalination. *Desalination* 538, 115903.
- Aende, A., Gardy, J., Hassanpour, A., 2020. Seawater desalination: a review of forward osmosis technique, its challenges, and future prospects. *Processes* 8 (8).
- Alturki, A.A., et al., 2013. Removal of trace organic contaminants by the forward osmosis process. *Sep. Purif. Technol.* 103, 258–266.
- Amjad, M., et al., 2018. Novel draw solution for forward osmosis based solar desalination. *Appl. Energy* 230, 220–231.
- Amjad, M., Haruna, M.A., Gardy, J., 2021. Chapter 2 - Nanomaterials for solar energy capture and steam generation. In: Ahmed, W., Booth, M., Nourafkan, E. (Eds.), *Emerging Nanotechnologies for Renewable Energy*. Elsevier, pp. 37–48.
- Bai, H., Liu, Z., Sun, D.D., 2011. Highly water soluble and recovered dextran coated Fe₃O₄ magnetic nanoparticles for brackish water desalination. *Sep. Purif. Technol.* 81 (3), 392–399.
- Ban, I., et al., 2019. Synthesis of poly-sodium-acrylate (PSA)-coated magnetic nanoparticles for use in forward osmosis draw solutions. *Nanomaterials* 9 (9), 1238.

- Bank, W., 2019. The Role of Desalination in an Increasingly Water-Scarce World. World Bank, p. 1 (Water Papers).
- Bell, E.A., Holloway, R.W., Cath, T.Y., 2016. Evaluation of forward osmosis membrane performance and fouling during long-term osmotic membrane bioreactor study. *J. Membr. Sci.* 517, 1–13.
- Cannon, J., et al., 2012. Influence of ion size and charge on osmosis. *J. Phys. Chem. B* 116 (14), 4206–4211.
- Cath, T.Y., et al., 2005. Membrane contactor processes for wastewater reclamation in space: Part I. Direct osmotic concentration as pretreatment for reverse osmosis. *J. Membr. Sci.* 257 (1), 85–98.
- Cath, T.Y., et al., 2010. A multi-barrier osmotic dilution process for simultaneous desalination and purification of impaired water. *J. Membr. Sci.* 362 (1–2), 417–426.
- Coday, B.D., et al., 2013. Effects of transmembrane hydraulic pressure on performance of forward osmosis membranes. *Environ. Sci. Technol.* 47 (5), 2386–2393.
- Collins, K.D., 1997. Charge density-dependent strength of hydration and biological structure. *Biophys. J.* 72 (1), 65–76.
- Dey, P., Izake, E.L., 2015. Magnetic nanoparticles boosting the osmotic efficiency of a polymeric FO draw agent: effect of polymer conformation. *Desalination* 373, 79–85.
- Fipps, G., *Irrigation water quality standards and salinity management strategies*. 2003.
- Fu, Y., et al., 2017. Investigation on enhancing effects of Au nanoparticles on solar steam generation in graphene oxide nanofluids. *Appl. Therm. Eng.* 114, 961–968.
- Hancock, N.T., Cath, T.Y., 2009. Solute coupled diffusion in osmotically driven membrane processes. *Environ. Sci. Technol.* 43 (17), 6769–6775.
- Hernández-Hernández, E., et al. Changing the surface characteristics of CNF, from hydrophobic to hydrophilic, via plasma polymerization with acrylic acid. in *Journal of Nano Research*. 2010. Trans Tech Publ.
- Khazaei, F., et al., 2021. Forward osmosis using highly water dispersible sodium alginate sulfate coated-Fe₃O₄ nanoparticles as innovative draw solution for water desalination. *Process Saf. Environ. Prot.* 146, 789–799.
- Kim, T.-w, et al., 2012. Systematic approach for draw solute selection and optimal system design for forward osmosis desalination. *Desalination* 284, 253–260.
- Kim, T.-w, Park, S., Yeh, K., 2013. Cost-effective design of a draw solution recovery process for forward osmosis desalination. *Desalination* 327, 46–51.
- Ling, M.M., Chung, T.-S., 2012. Surface-dissociated nanoparticle draw solutions in forward osmosis and the regeneration in an integrated electric field and nanofiltration system. *Ind. Eng. Chem. Res.* 51 (47), 15463–15471.
- Long, Q., et al., 2018. Recent advance on draw solutes development in forward osmosis. *Processes* 6 (9), 165.
- Ma, X., et al., 2021. Polypyrrole–dopamine nanofiber light-trapping coating for efficient solar vapor generation. *ACS Appl. Mater. Interfaces* 13 (48), 57153–57162.
- Mazlan, N.M., Peshev, D., Livingston, A.G., 2016. Energy consumption for desalination — a comparison of forward osmosis with reverse osmosis, and the potential for perfect membranes. *Desalination* 377, 138–151.
- McCormick, P., et al., 2008. Water, salt, and ethanol diffusion through membranes for water recovery by forward (direct) osmosis processes. *J. Membr. Sci.* 325 (1), 467–478.
- McCutcheon, J., Elimelech, M., 2007. Modeling water flux in forward osmosis: implications for improved membrane design. *AIChE J.* 53, 1736–1744.
- McCutcheon, J.R., McGinnis, R.L., Elimelech, M., 2005. A novel ammonia–carbon dioxide forward (direct) osmosis desalination process. *Desalination* 174 (1), 1–11.
- McGinnis, R.L., Elimelech, M., 2007. Energy requirements of ammonia–carbon dioxide forward osmosis desalination. *Desalination* 207 (1), 370–382.
- Nandiyanoto, A.B.D., Oktiani, R., Ragadhita, R., 2019. How to read and interpret FTIR spectroscopy of organic material. *Indones. J. Sci. Technol.* 4 (1), 97–118.
- Ni, G., et al., 2015. Volumetric solar heating of nanofluids for direct vapor generation. *Nano Energy* 17, 290–301.
- Organization, W.H., *Drinking water parameter cooperation project: support to the revision of Annex I council directive 98/83/EC on the quality of water intended for human consumption (Drinking Water Directive)*. no. September, 2017: p. 1–228.
- Pavia, D.L., et al., 2014. *Introduction to Spectroscopy*. Cengage learning.
- Pegasusweb. *Climate - Leeds (England)*. 2022 07/11/2022 [cited 2022 07/11/2022]; Available from: (<https://www.climatestotravel.com/climate/england/leeds>).
- Phuntsho, S., et al., 2013. Assessing the major factors affecting the performances of forward osmosis and its implications on the desalination process. *Chem. Eng. J.* 231, 484–496.
- Shaffer, D.L., et al., 2015. Forward osmosis: where are we now? *Desalination* 356, 271–284.
- Wang, X., et al., 2016a. Direct vapor generation through localized solar heating via carbon-nanotube nanofluid. *Energy Convers. Manag.* 130, 176–183.
- Wang, X., et al., 2016b. Graphene-based recyclable photo-absorbers for high-efficiency seawater desalination. *ACS Appl. Mater. Interfaces* 8 (14), 9194–9199.
- Zhao, S., Zou, L., 2011. Relating solution physicochemical properties to internal concentration polarization in forward osmosis. *J. Membr. Sci.* 379 (1), 459–467.
- Zou, S., et al., 2016. Energy consumption by recirculation: a missing parameter when evaluating forward osmosis. *Environ. Sci. Technol.* 50 (13), 6827–6829.
- Zou, S., Qin, M., He, Z., 2019. Tackle reverse solute flux in forward osmosis towards sustainable water recovery: reduction and perspectives. *Water Res.* 149, 362–374.